

Suzaku Observation of HCG 62: Temperature, Abundance, and Extended Hard X-ray Emission Profiles

Kazuyo TOKOI,¹ Kosuke SATO,² Yoshitaka ISHISAKI,¹ Takaya OHASHI,¹ Noriko Y. YAMASAKI,³
 Kazuhiro NAKAZAWA,⁴ Kyoko MATSUSHITA,² Yasushi FUKAZAWA,⁵ Akio HOSHINO,¹
 Takayuki TAMURA,³ Chihiro EGAWA,⁵ Naomi KAWANO,⁵ Naomi OTA,³ Naoki ISOBE,⁶
 Madoka KAWAHARADA,⁶ Hisamitsu AWAKI,⁷ and John P. HUGHES⁸

¹*Department of Physics, Tokyo Metropolitan University, 1-1 Minami-Osawa, Hachioji, Tokyo 192-0397*

²*Department of Physics, Tokyo University of Science, 1-3 Kagurazaka, Sinjuku-ku, Tokyo 162-8601*

³*Institute of Space and Astronautical Science (ISAS),*

Japan Aerospace Exploration Agency, 3-1-1 Yoshinodai, Sagami-hara, Kanagawa 229-8510

⁴*Department of Physics, University of Tokyo, Hongo 7-3-1, Bunkyo-ku, Tokyo 113-0033*

⁵*Department of Physical Science, Hiroshima University,*

1-3-1 Kagamiyama, Higashi-Hiroshima, Hiroshima 739-8526

⁶*Cosmic Radiation Laboratory, RIKEN, 2-1 Hirosawa, Wako, Saitama 351-0198, Japan*

⁷*Department of Physics, Ehime University, 2-5 Bunkyo-machi, Matsuyama-shi, Ehime 790-8577*

⁸*Department of Physics and Astronomy, Rutgers University,*

136 Frelinghuysen Road, Piscataway, NJ 08854-8019, USA

(Received 0 0; accepted 0 0)

Abstract

We present results of 120 ks observation of a compact group of galaxies HCG 62 ($z=0.0145$) with Suzaku XIS and HXD-PIN. The XIS spectra for four annular regions were fitted with two temperature *vap*ec model with variable abundance, combined with the foreground Galactic component. The Galactic component was constrained to have a common surface brightness among the four annuli, and two temperature *ap*ec model was preferred to single temperature model. We confirmed the multi-temperature nature of the intra-group medium reported with Chandra and XMM-Newton, with a doughnut-like high temperature ring at radii 3.3–6.5' in a hardness image. We found Mg, Si, S, and Fe abundances to be fairly robust. We examined the possible “high-abundance arc” at $\sim 2'$ southwest from the center, however Suzaku data did not confirm it. We suspect that it is a misidentification of an excess hot component in this region as the Fe line. Careful background study showed no positive detection of the extended hard X-rays previously reported with ASCA, in 5–12 keV with XIS and 12–40 keV with HXD-PIN, although our upper limit did not exclude the ASCA result. There is an indication that the X-ray intensity in $r < 3.3'$ region is

$70 \pm 19\%$ higher than the nominal CXB level (5–12 keV), and Chandra and Suzaku data suggest that most of this excess could be due to concentration of hard X-ray sources with an average photon index of $\Gamma = 1.38 \pm 0.06$. Cumulative mass of O, Fe and Mg in the group gas and the metal mass-to-light ratio were derived and compared with those in other groups. Possible role of AGN or galaxy mergers in this group is also discussed.

Key words: galaxies: clusters: individual (HCG 62) — galaxies: intergalactic medium — galaxies: abundances — galaxies: interactions — X-rays: galaxies: clusters — X-rays: diffuse background

1. Introduction

Groups of galaxies play a key role in the formation of the universe. Most importantly, they act as building blocks in the framework of hierarchical formation of structures (e.g. Navarro et al. 1995). In this sense, properties of groups should be critically compared with those in clusters of galaxies, to test the general hypothesis that groups of galaxies indeed represent the condition in clusters when they have not been evolved. For example, baryon to dark matter ratio and metal abundance in groups of galaxies can be a measure to be tested whether rich clusters are indeed simple superposition of many groups or some other mechanism may be involved.

The groups are characterized by a short dynamical time scale, and we expect galaxy encounters to take place frequently in such a high density environment. The X-ray search for an evidence of dynamical processes in the form of hard non-thermal emission would be an important subject of observational studies. The relatively low gas temperature compared with rich clusters greatly helps us find such emission even with standard CCD instruments. Also it is well known that group gas tends to contain significantly high entropy if one extrapolates the scaling relation holding for clusters (Ponman et al. 1999). A simulation study indicated that simple galactic winds were unable to significantly raise the entropy in cluster size hot gas (Borgani et al. 2005). This indicates that a certain heat input or preheating occurred over a widespread region and groups of galaxies offer us an opportunity to closely look into such an effect.

Another aspect concerning groups of galaxies is their role in the chemical enrichment of cluster hot gas. It has been shown that rich clusters maintain all the metals produced by the cluster galaxies (Fukazawa et al. 1998), however early-type galaxies are thought to have released most of the metals formed through past supernova explosions (Makishima et al. 2001). We should note that these galaxies almost always reside in groups and clusters of galaxies and that their X-ray haloes may not be clearly separable from the surrounding gas. Groups

of galaxies lie in the region where the metal confinement can be marginally possible. This means that by looking into the distribution of various metals in groups, we can measure the efficiency of metal confinement and further estimate how each metal has been injected into the intergalactic space. The low temperature (< 2 keV) of the group gas also greatly helps us study emission lines from various metals ranging from oxygen to iron.

HCG 62 is one of the brightest and well-studied groups of galaxies among the Hickson compact groups of galaxies (Hickson et al. 1989) located at $z = 0.0145$ (Mulchaey et al. 2003). Zabludoff & Mulchaey (2000) extensively surveyed a 1.5×1.5 deg² region around the group and measured redshifts of 154 galaxies. They identified 63 of them as members of the group within a radius of $50'$ (900 kpc), and the measured velocity dispersion, $\sigma_r = 390^{+37}_{-34}$ km s⁻¹, is a typical value for galaxy groups. The central region within $r < 1.1'$ is dominated by three galaxies, HCG 62a (NGC 4778), HCG 62b (NGC 4776), and HCG 62c (NGC 4761), and they are all classified as S0 galaxies. Kinematics of these galaxies suggests possible interaction among them (Spavone et al. 2006; Rampazzo et al. 1998). Such a high galaxy density and the low velocity dispersion are considered to result in a galaxy merger, and Ponman & Bertram (1993) suggested that they should culminate in a final merger within a few billion years, consisting of a large elliptical galaxy embedded in an extended X-ray halo.

HCG 62 is also known as the first compact galaxy group that was detected in X-ray to have an extended hot gas (intra-cluster or group medium; ICM), and the ICM properties have been extensively studied using ROSAT and ASCA (e.g., Ponman & Bertram 1993; Pildis et al. 1995; Finoguenov & Ponman 1999; Mulchaey et al. 2003). Furthermore, spatially extended hard X-ray excess over the ICM emission was detected with ASCA (Fukazawa et al. 2001; Nakazawa et al. 2007), and two symmetrical cavities in the central region at a projected radius of $\sim 25''$ (7.4 kpc) were discovered by Chandra (Vrtilek et al. 2002). Detailed hot-gas properties including the cavities and the gravitational mass have been studied based on the combined data from Chandra and XMM-Newton (Morita et al. 2006). Recently, Gu et al. (2007) reported that a region at $2'$ offset from the central galaxy showed a twice higher metal abundance than the surrounding gas (the “high-abundance arc”).

In this paper, we report the results from Suzaku observation of HCG 62. Owing to the low and stable background as well as good sensitivity to emission lines below ~ 1 keV of the X-ray Imaging Spectrometer (XIS; Koyama et al. 2007), accurate determination of O and Mg abundances to outer regions have become feasible. XIS is also effective to constrain the extended hard X-ray emission in combination with the Hard X-ray Detector (HXD; Takahashi et al. 2007). This paper is organized as follows: In sections 2 and 3, we describe the Suzaku observation and the data reduction, and show images of HCG 62 obtained with Suzaku in section 4. In sections 5–7, we describe spectral analysis and the derived temperature and abundance profiles, and examine the existence of the “high-abundance arc” in section 8. In section 9, significance of the extended hard X-ray emission with Suzaku is carefully investigated. We discuss temperature

Table 1. Suzaku observation log of HCG 62.

| | | | |
|---------------------------------|---|------------------|---------------------------|
| Observation ID | 800013020 | | |
| Target Coordinates (J2000) | (RA_NOM, DEC_NOM) = (12 ^h 53 ^m 06 ^s , −9°12′14″) | | |
| Date of Observation | 2006 January 20, 09:19 – 23, 12:00 | | |
| Exposure Time | XIS: 119.3 ks | HXD-PIN: — | (No <i>COR</i> selection) |
| | XIS: 85.4 ks | HXD-PIN: 75.1 ks | (<i>COR</i> > 8 GV) |

and metallicity distributions, metal mass-to-light ratio, and galaxy mergers in section 10, and a summary is given in section 11.

We use $H_0 = 0.7 h_{100} = 70 \text{ km s}^{-1} \text{ Mpc}^{-1}$, $\Omega_\Lambda = 1 - \Omega_M = 0.73$ throughout this paper. At the redshift of $z = 0.0145$, 1′ corresponds to 17.8 kpc. The virial radius, $r_{180} \equiv 1.95 h_{100}^{-1} \sqrt{k\langle T \rangle / 10 \text{ keV}} = 1.08 \text{ Mpc}$ (Markevitch et al. 1998; Evrard et al. 1996) for the average temperature of $k\langle T \rangle = 1.5 \text{ keV}$. We adopt a Galactic hydrogen column density of $N_H = 3.03 \times 10^{20} \text{ cm}^{-2}$ in the direction of HCG 62 (Dickey & Lockman 1990). As for the definition of the solar abundance ratio, we followed Anders & Grevesse (1989). Errors are 90% confidence range for a single interesting parameter.

2. Observation

Suzaku carried out observation of the central part of HCG 62 in January 2006 as a part of the Science Working Group (SWG) time. The observation log is shown in table 1. The XIS instrument was set to the normal clocking mode with data formats of 5×5 and 3×3 editing modes. See Koyama et al. (2007) for details of the operation mode. The XIS images are shown in figure 1. We used the version 0.7 processing data, and the analysis was performed with HEASoft 6.1.1 and XSPEC 11.3.2t. After applying the standard data selection criteria: elevation from the sunlit Earth rim, $DYE_ELV > 20^\circ$, elevation from the Earth rim, $ELV > 5^\circ$, time after the South Atlantic Anomaly (SAA) passage, $T_SAA_HXD > 256 \text{ s}$, the exposure time of XIS was 119.4 ks. Events of bad CCD event grades, bad columns, and hot/flickering pixels were removed, by choosing $GRADE = 0, 2, 3, 4$, or 6 , $STATUS < 262144$, and applying “sisclean” FTOOLS.

The HXD PIN and PMT were operated with nominal high-voltage supply and setups (Kokubun et al. 2007). From the background modeling limitations as of the beginning of 2006, we selected time regions with the magnetic cut-off rigidity (*COR*) larger than 8 GV, and $T_SAA_HXD > 1000 \text{ s}$. With these screenings, we obtained 75.1 ks of exposure for the PIN detector. We did not analyze the GSO data of the HXD instrument in this paper.

Table 2. Area, coverage of whole annulus, SOURCE_RATIO_REG, and observed/estimated counts for each annular region. SOURCE_RATIO_REG represents the flux ratio in the assumed spatial distribution on the sky (3β -model) inside the accumulation region to the entire model, and written in the header keyword of the calculated ARF response by “xissimarfgen”.

| Region [*] | Area [†] (arcmin ²) | Coverage [†] | SOURCE_RATIO_REG [‡] | Energy (keV) | BI counts [§] | | | | FI counts [§] | | | |
|---------------------|---|-----------------------|-------------------------------|-----------------|------------------------|-------|-------|------------------|------------------------|-------|-------|------------------|
| | | | | | OBS | NXB | CXB | f_{BGD} | OBS | NXB | CXB | f_{BGD} |
| 0.0–3.3′ | 33.4 | 100.0% | 51.3% | 0.4–7.5 | 35,067 | 906 | 1,020 | 5.5% | 65,887 | 1,445 | 2,353 | 5.8% |
| 3.3–6.5′ | 100.1 | 100.0% | 16.8% | 0.4–7.5 | 20,095 | 2,691 | 2,620 | 26.4% | 34,990 | 3,944 | 5,966 | 28.3% |
| 6.5–9.8′ | 147.1 | 88.2% | 13.5% | 0.4–7.5 | 16,943 | 3,674 | 2,902 | 38.8% | 27,659 | 5,256 | 6,251 | 41.6% |
| 9.8–13′ | 36.8 | 15.8% | 2.1% | 0.4–4.0 | 2,726 | 629 | 492 | 41.1% | 4,523 | 980 | 1,051 | 44.9% |
| $r < 1.1′$ | 3.8 | 100.0% | 33.2% | 0.4–7.5 | 11,191 | 105 | 120 | 2.0% | 22,794 | 166 | 279 | 2.0% |
| NE arc | 14.8 | 100.0% | 9.0% | 0.4–7.5 | 10,420 | 405 | 451 | 8.2% | 20,389 | 650 | 1,045 | 8.3% |
| SW arc | 14.8 | 100.0% | 9.0% | 0.4–7.5 | 13,358 | 416 | 433 | 6.4% | 22,526 | 646 | 1,011 | 7.4% |

^{*} See figure 1(a) for the first four annuli, figure 7(a) for the latter three.

[†] The average values among four sensors are presented.

[‡] SOURCE_RATIO_REG \equiv COVERAGE $\times \int_{r_{\text{in}}}^{r_{\text{out}}} S(r) r dr / \int_0^\infty S(r) r dr$, where $S(r)$ represents the assumed radial profile of HCG 62, and we defined $S(r)$ in $26′ \times 26′$ region on the sky.

[§] OBS denotes the observed counts including NXB and CXB in 0.4–7.5 keV or 0.4–4 keV. NXB and CXB are the estimated counts.

3. Data Reduction

In this section, we describe the spectral analysis of the ICM with XIS. First we extracted spectra from four annular regions of 0.0–3.3′, 3.3–6.5′, 6.5–9.8′, and 9.8–13′, centered on the target coordinates in table 1. As for the background, we assumed a nominal cosmic X-ray background (CXB) spectrum with a power-law photon index, $\Gamma = 1.4$, and surface brightness of $5.97 \times 10^{-8} \text{ erg cm}^{-2} \text{ s}^{-1} \text{ sr}^{-1}$ in 2–10 keV (Kushino et al. 2002). The non X-ray background (NXB) spectra were estimated from a database of the dark Earth observations with Suzaku for the same detector area and with the same distribution of COR (Tawa et al. 2007). In order to increase the signal to noise ratio by reducing the NXB count rate, especially for the group outskirts and in high energy bands ($E \gtrsim 4 \text{ keV}$), we further required $COR > 8 \text{ GV}$ for the spectral analysis. After this screening, the exposure time dropped to 85.4 ks, however, the fit residuals in higher energy band were reduced and the spectral fits became almost acceptable as described in a later section.

In figure 2, spectra of the back-illuminated sensor (BI = XIS1) and sum of three front-illuminated sensors (FI = XIS0, XIS2, XIS3) for four annular regions after the background subtraction are presented. The estimated spectra of the CXB and NXB are overlaid. Uncertainty in the CXB spectrum is $\sim 10\%$ or more (Kushino et al. 2002) depending on the accumulation area of the spectrum, and the reproducibility of the NXB is $\lesssim 5\%$ for 100 ks observation spanning 2–3 days (Tawa et al. 2007). The ^{55}Fe calibration source regions at two CCD corners

Table 3. Estimated fractions of the ICM photons accumulated in the annular detector regions coming from the corresponding sky by “xissim” simulation for BI (XIS1) at 1 keV. These numbers are not much different ($\lesssim 1\%$) for other sensors and the examined energy bands.

| Detector | Sky Region | | | | |
|----------|------------|----------|----------|---------|-----------|
| Region | 0.0–3.3′ | 3.3–6.5′ | 6.5–9.8′ | 9.8–13′ | $r > 13′$ |
| 0.0–3.3′ | 95.6% | 4.4% | 0.0% | 0.0% | 0.0% |
| 3.3–6.5′ | 17.2% | 68.6% | 14.1% | 0.0% | 0.0% |
| 6.5–9.8′ | 0.2% | 8.2% | 81.3% | 10.2% | 0.0% |
| 9.8–13′ | 0.0% | 0.2% | 8.8% | 90.0% | 1.0% |

were included when we accumulated spectral data for the 9.8–13′ annulus, however the energy range of the fit was limited to 0.4–4 keV. The calibration source regions in the 6.5–9.8′ annulus were excluded, and the fitting energy range was set at 0.4–7.5 keV for 0.0–3.3′, 3.3–6.5′, and 6.5–9.8′ annuli. In addition, the energy range around the Si K-edge (1.825–1.840 keV) was ignored in the spectral fit. Table 2 summarizes area, coverage, energy range, and the BI and FI counts for the observed spectra and the estimated NXB and CXB spectra. The fraction of the background, $f_{\text{BGD}} \equiv (\text{NXB} + \text{CXB})/\text{OBS}$, was less than 50% even at the outermost annulus, although the Galactic component is not considered here.

The response of the XRT and XIS were calculated by “xissimarfgen” version 2006-08-26 ancillary response file (ARF) generator (Ishisaki et al. 2007) and “xisrmfgen” version 2006-10-26 response matrix file (RMF) generator. Slight degradation of the energy resolution was considered in the RMF, and decrease of the low energy transmission of the XIS optical blocking filter (OBF) was included in the ARF. The ARF response was calculated assuming a surface brightness profile, $S(r)$, based on the combined analysis of Chandra and XMM-Newton data in 0.5–4 keV within $r < 14′$. The profile is described by a 3β -model, which is given in table 3 of Morita et al. (2006). Fraction of the assumed intensity from the corresponding sky region for each annulus is presented in the `SOURCE_RATIO_REG` column of table 2. We also checked the fraction of events coming from near-by regions other than the corresponding sky for each annulus using the “xissim” simulator (Ishisaki et al. 2007), as shown in table 3. The stray fraction was not significant and less than 1/3 in the worst case. The deprojection analysis was not conducted in this paper, however, we have confirmed that this analysis would not change the best-fit parameters significantly.

4. X-ray Image

The XIS images in 0.5–4 keV and 6–10 keV are shown in figure 1(a) and (b). Estimated contributions of NXB and CXB were subtracted and exposure was corrected, but no vignetting correction was applied. Magnified image of the central region in 0.5–4 keV without gaussian

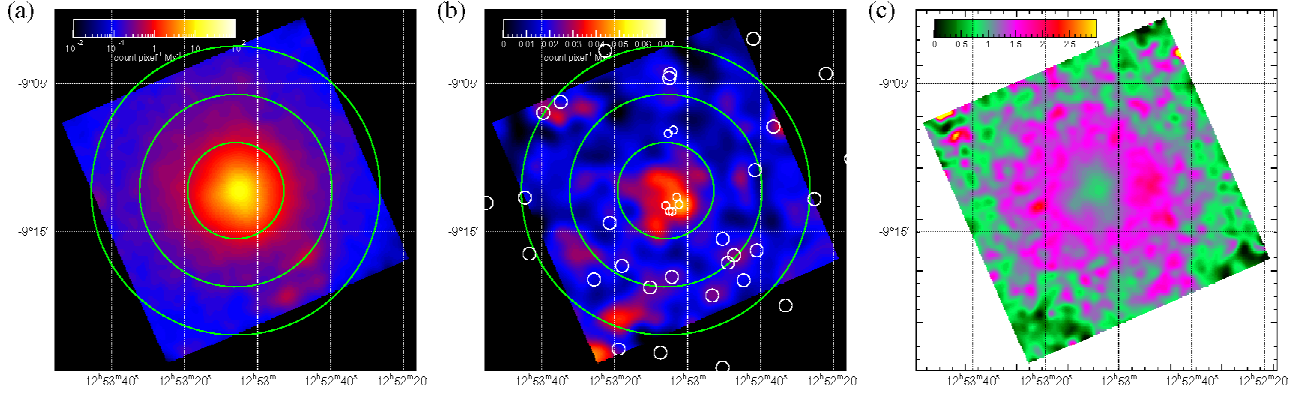


Fig. 1. (a) Exposure corrected XIS image in 0.5–4.0 keV, (b) in 6–10 keV energy range, and (c) hardness ratio image of 1–2 keV to 0.5–1 keV bands. Images of (a) and (c) are smoothed with gaussian of $\sigma = 17''$, and (b) is with $\sigma = 33''$. Estimated components of the NXB and CXB are subtracted, but no vignetting correction is applied. Green circles corresponds to 3.3', 6.5', and 9.8' radii, from inner to outer, centered on HCG 62. No *COR* selection is applied, and both BI and FI sensors are co-added, in order to maximize the photon statistics. The ^{55}Fe calibration source areas at corners are included in (a) and (c), but excluded in (b). White circles in (b) represent locations of point sources detected by XMM-Newton. Sources shown in smaller circles are also detected with Chandra.

smoothing is also shown in figure 7(a), which will be discussed in section 8. There is a slight positional shift of the X-ray peak by less than $\sim 0.3'$ from the region center, due to the source position error of $19''$ corresponding to the 90% error circle radius of Suzaku telescopes after the astrometry correction for the thermal distortion of the spacecraft (Uchiyama et al. 2007). Though this astrometry correction was not incorporated in our analysis, the shift of the average pointing direction due to the thermal distortion is estimated to be $6.4''$ which gives a minor effect.

The 0.5–4 keV image is dominated by the ICM emission, however intensity gradient becomes weaker at the outer two annuli, where the Galactic emission has comparable intensity. In 6–10 keV, the thermal ICM emission can hardly be seen as shown in figure 1(b), which is a linear-scale plot of the intensity. However, some extended emission can be seen within $r < 3.3'$. It is notable that this emission seems elongated along the direction of the two cavities ($32''$ north-east and $20''$ south-west) which were observed with Chandra (Vrtilek et al. 2002; Morita et al. 2006). There are other extended hard emissions which do not match point sources (white circles) as detected with XMM-Newton. The statistical significance of the hard X-ray emission is discussed in section 9.

Figure 1(c) shows a hardness ratio image based on the 1–2 keV and 0.5–1 keV intensities. Although the vignetting correction was not performed, the two energy bands show very similar vignetting features. The transmission degradation due to the OBF contaminant is not corrected for either, which is larger for the 0.5–1 keV band and at the central part of the CCD. Therefore the hardness ratio shows a systematic drop from the center to outer regions for a constant

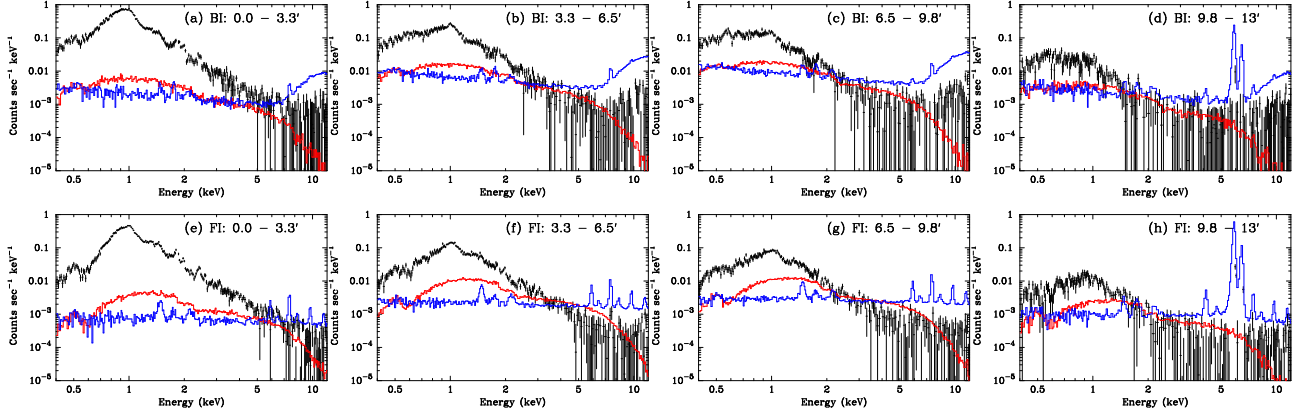


Fig. 2. The observed spectra at the annular regions for (a)–(d) BI and (e)–(h) FI sensors. Estimated components of the NXB and CXB are subtracted, which are indicated by blue and red histograms. The $COR > 8$ GV screening is applied. The ^{55}Fe calibration source areas are included for the accumulation regions of (d) and (h), but excluded for others.

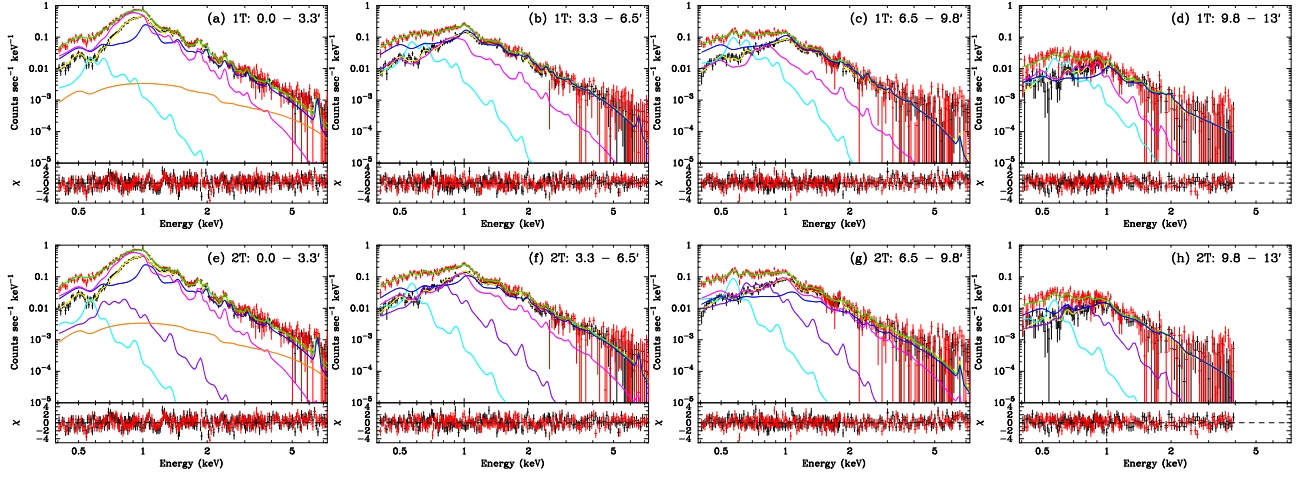


Fig. 3. The observed spectra are plotted by red and black crosses for BI and FI, respectively, and they are simultaneously fitted with (a)–(d) Gal 1T: $constant \times [phabs \times (vapec + vapec) + apec]$, or (e)–(h) Gal 2T: $constant \times [phabs \times (vapec + vapec) + apec + apec]$ model, drawn by green and yellow lines for the BI and FI spectra. The hot and cool ICM components (two *vapec*) for the BI spectra correspond to magenta and blue lines. The *apec* component(s) for the BI spectra are indicated by cyan (and purple) line(s). The spectral fit was conducted in the energy range of 0.4–7.5 keV for (a)–(c) and (e)–(g), and 0.4–4 keV for (d) and (h). The energy range around the Si K-edge (1.825–1.840 keV) was ignored in the spectral fit. The lower panels show the fit residuals in unit of σ .

temperature distribution. In the hardness image, there is a clear doughnut-like structure with high hardness ratio around the annulus of 3.3–6.5'. This is due probably to a relative dominance of the high temperature component in the ICM which is mostly occupied by the cool component at the group core, as already reported by Morita et al. (2006). They also found a sharp temperature drop from $kT_{\text{Hot}} \sim 1.5$ keV at $r \sim 3'$ to ~ 0.6 keV at $r \sim 10'$, which may well form the doughnut-like hot structure. However, the Galactic component becomes comparable to the

ICM in the outer annuli, so the overall temperature structure needs to be examined in detail.

5. Spectral Analysis

We have carried out spectral fits to the observed spectra in the four annular regions. The estimated NXB and CXB were subtracted from the spectra, but we estimate the parameter error ranges by adjusting these background intensities by $\pm 10\%$. The fitting model consists of the following components.

1. Galactic Hot Gas: we tried both single (Gal 1T; kT_{Gal}) and two temperature (Gal 2T; kT_{G1} , kT_{G2}) models for this component. In both models, surface brightness were constrained to be equal among the four annuli, and *apec* models with solar abundance at $z = 0$ were utilized. When single temperature was assumed, the common temperature over the four annuli and its surface brightness were varied as two free parameters. In the two temperature case, we had to fix both the temperatures because of strong coupling with the ICM temperatures. Based on the previous reports (e.g., Lumb et al. 2002; Kuntz & Snowden 2000; Snowden et al. 1997), we assumed $kT_{\text{G1}} = 0.138$ keV attributed to the Local Hot Bubble and $kT_{\text{G2}} = 0.344$ keV as the Milky-Way Halo, respectively. The intensities of these two components were varied as free parameters. Though these temperatures are slightly higher than those obtained with ROSAT (Kuntz & Snowden 2000) or XMM-Newton (Lumb et al. 2002), we chose the values which gave the largest difference from the Gal 1T results within the ROSAT error range. We also note that the location of HCG 62, $(l, b) = (303^\circ, 54^\circ)$ in the Galactic coordinate, is within $\sim 15^\circ$ from the Galactic Bulge and the North Polar Spur – Loop I (Snowden et al. 1995). Influence of the assumed temperatures on the ICM abundance is examined in section 7.

2. Low-Mass X-ray Binaries (LMXBs): the discrete source contribution in member galaxies of HCG 62 was included only for 0.0–3.3' annulus, assuming thermal bremsstrahlung emission, *zbrems*, at $z = 0.0145$ with a fixed temperature of $kT = 7$ keV and fixed intensity. The intensity, $F_X = 9.3 \times 10^{-14}$ erg cm $^{-2}$ s $^{-1}$ (0.3–8 keV), employed here is based on the Chandra results by Kim & Fabbiano (2004), in which the integrated LMXB luminosity, L_X , was related to the B band optical luminosity, L_B , as

$$L_X/L_B = (0.9 \pm 0.5) \times 10^{30} \text{ erg s}^{-1}/L_{B\odot}. \quad (1)$$

3. ICM in HCG 62: we assumed two temperature (kT_{Hot} , kT_{Cool}) optically-thin thermal plasma model, *vapec*, at $z = 0.0145$ for ICM based on the previous Chandra and XMM-Newton studies (Morita et al. 2006). As an exception, only single temperature was considered in the Gal 2T model for the outermost annulus (9.8–13'), because we could not constrain kT_{Hot} . As for the metal abundance, we grouped relevant metals into six groups, namely, Mg and Al; S, Ar and Ca; Fe and Ni were combined, and O, Ne and Si were varied individually.

Consequently, Gal 1T: $\text{constant} \times [\text{phabs} \times (\text{vapec} + \text{vapec}) + \text{apec}]$, or Gal 2T: $\text{constant} \times [\text{phabs} \times (\text{vapec} + \text{vapec}) + \text{apec} + \text{apec}]$ model was adopted for the spectral fit. The *phabs* factor

denotes the Galactic absorption due to neutral atoms, and the hydrogen column density was fixed to $N_{\text{H}} = 3.03 \times 10^{20} \text{ cm}^{-2}$ (Dickey & Lockman 1990). Note that this absorption model is also affected by the assumed solar abundance table as discussed in Appendix 2 of Sato et al. (2007). In order to constrain the surface brightness of the Galactic component, a total of 8 spectra, with BI and FI sensors for the four annuli, were simultaneously fitted. The *constant* factor was introduced to compensate the possible flux discrepancy between the BI and FI sensors, however, it turned out to be unity within $\pm 5\%$.

The fitted spectra are presented in figure 3, and the best-fit parameters are summarized in table 4. Flux and normalization in the table are for the FI spectra. The reduced χ^2 values are $\simeq 1.2$ for the two models, and slightly better for the Gal 2T model with $\Delta\chi^2 = 15$. Both models are statistically rejected if we consider only the statistical errors, however, they become acceptable when systematic error of 5% is added in each bin. The reduced χ^2 is particularly large in the innermost region ($r < 3.3'$), where temperature gradient was observed with Chandra (Morita et al. 2006). The residuals of the fit show large scatter around 1–1.5 keV in figure 3(a) and (e). This is presumably because the Fe-L line complex of multi-temperature ICM is not well-fitted by the simple two temperature *vaptec* model. We will further describe the results on temperature and metal abundance separately.

6. Temperature Profile

Radial temperature profile and the ratio of the *vaptec* normalizations between hot and cool ICM components are shown in figure 4(a) and (b). The different models of the Galactic emission (1T or 2T) gave a difference in ICM temperature by about 0.5 keV for the hot and cool ICM components, except for the innermost region. Though the previous Chandra and XMM-Newton result seems to be consistent with the Gal 1T case, the Galactic component had been neglected in that analysis. Very crudely, $kT_{\text{Hot}} \sim 1.5 \text{ keV}$, and $kT_{\text{Cool}} \sim 0.8 \text{ keV}$. The cool component is strongest in the innermost region, and even though it seems to decline in the outer regions, the possible coupling with the Galactic emission makes the precise estimation difficult. The radius of $10' \sim 180 \text{ kpc}$ corresponds to $\sim 0.16 r_{180}$, and the temperature decline, observed in several other clusters, is not clearly recognized in this system due partly to the multi-phase nature of ICM. However, hardening of the spectra at the 3.3–6.5' annulus and softening in the outer two annuli suggested by the hardness ratio image in figure 1(c) is evident in figure 4(a) and (b) for both models of the Galactic emission.

Figure 4(c) show the surface brightness profile with Suzaku for the Gal 2T model, compared with the 3β -model obtained with Chandra and XMM-Newton (Morita et al. 2006). The observed profiles look almost consistent with this model, while the Suzaku intensity for the Gal 1T model is slightly higher at the outermost annulus. We note that, although the surface brightness of the hot ICM component decreases steeply, the cool component stays almost constant at $r > 3.3'$. The intensity is comparable to the Galactic component, $S_{\text{G1+G2}}$, and it is

very difficult to separate these two components clearly. Further offset observations with Suzaku and/or high resolution spectroscopy with, e.g., microcalorimeters, are anticipated.

We have estimated the systematic errors caused by the background subtraction and by the estimation of the XIS filter contamination. We varied the sum of the NXB and CXB by $\pm 10\%$, and the contamination thickness by $\pm 20\%$, respectively. The results are shown by dotted lines for the Gal 2T model in figure 4(a). The impact on the temperature is generally less than the systematic temperature shift, particularly on kT_{Cool} , with the different models of the Galactic emission. On the other hand, kT_{Hot} is much affected by the background uncertainty most notably in the 6.5–9.8′ annulus, where the hot-component intensity is comparable to the Galactic emission and CXB, as seen in figure 4(c).

7. Abundance Profile

Metal abundances are determined for the six element groups individually as shown in figures 5(a)–(f). O abundance is strongly affected by how we model the Galactic emission. The two cases give largely different abundance values up to 0.3 solar in the regions of $r > 3.3'$, although they overlap within 90% statistical errors. Figures 6(a)–(i) show confidence contours between O abundance for the inner three annuli and the Galactic temperatures. In the Gal 2T model, either of the two temperatures was fixed to the assumed value when we calculated the contours. Only for the group center region, we obtained a tight and consistent value of 0.35 ± 0.08 solar (Gal 2T case). The assumed temperatures are slightly lower or higher than the temperatures at the χ^2 -minimum for the kT_{G1} or kT_{G2} case, respectively, and give higher O abundance, though it is only at 1σ level. Gal 2T model gives higher O abundance than Gal 1T case in the outer three annuli, however O abundance is less than 0.32 solar at the 90% confidence excluding the outer most annulus which has large statistical errors. Thus spatial profile of O abundance is likely to be almost flat or declining with the radius.

We note that Ne abundance has a problem in the spectral fit due to the coupling with Fe-L feature. Therefore, regarding the spatial structure, we deal with the remaining four elemental groups: Mg, Si, S and Fe. The four abundance results look quite similar to each other, including the central value and the radial gradient. The central abundances are between 0.8–1.2 solar, and the abundances decline to about 1/5 of the central value in the 6.5–9.8′ annulus. Note also that the abundance results for the four elements in $r < 9.8'$ all agree within 15% between the two choices of the Galactic component, even though the resultant temperatures exhibit large discrepancy as seen in figure 4(a). This indicates that these abundance results are fairly robust.

Again, we looked into the effect of the errors in the NXB and CXB intensities and the OBF contamination thickness. As shown by dotted lines in figures 5(a)–(f), the systematic effect is less than the statistical error for all regions. Our Suzaku results are also consistent with the previous results with Chandra and XMM-Newton plotted with gray crosses. However, errors are much smaller in the outer three annuli, owing to much deeper exposure and good

sensitivity of Suzaku XIS.

8. Does “High-Abundance Arc” Exist?

Gu et al. (2007) reported that there was a high-abundance arc region at about $2'$ from the X-ray peak spanning from south to northwest, and a part of it roughly coincides with the outer edge of the southwest X-ray cavity. The reported abundance result with Chandra ACIS-S3 as $0.84^{+0.19}_{-0.15}$ solar in the radial range $1.77\text{--}2.21'$ of southwest half arc (region B+C in table 1 of Gu et al. 2007). The abundance was even higher than the level at the group center ($r < 0.44'$). The projected $0.7\text{--}7$ keV spectrum was fitted with a single absorbed *apec* model with the absorption fixed to the Galactic value. They used the solar abundance table of Grevesse & Sauval (1998), where the iron number abundance relative to hydrogen is 3.16×10^{-5} , which is less than our value of 4.68×10^{-5} by Anders & Grevesse (1989).

In order to confirm the “high-abundance arc” with Suzaku, we split the central $0.0\text{--}3.3'$ region into three parts; $r < 1.1'$, northeast (NE) arc, and southwest (SW) arc, respectively, as shown in figure 7(a). The extracted spectrum for each region and the best-fit parameters with the Gal 2T model are presented in figures 7(b)–(d) and table 5. Area, coverage, and observed/estimated counts are given in table 2. In the spectral fit, the Galactic and LMXB components were fixed to the same shape as in the previous fit for the $0.0\text{--}3.3'$ region with the same surface brightness. We note that the modeling of the Galactic component does not affect the best-fit results in this region, as shown in figures 4 and 5.

Though we confirmed the abundance gradient in $r < 3.3'$ as suggested by Morita et al. (2006), no excess abundance larger than the central $r < 1.1'$ region was observed in SW arc which contains the “high-abundance arc”. Comparing NW and SW arcs, SW one tend to show slightly higher value, although their 90% error ranges of the abundances overlap. One outstanding feature in SW arc is that the intensity of the hot ICM component is much higher than the cool one among the three regions examined, as seen in figure 7(d) with blue and magenta lines.

Since the angular resolution of Suzaku ($\sim 2'$ in half power diameter; Serlemitsos et al. 2007) is much worse than that of Chandra ($\lesssim 1''$), X-ray emission from the “high-abundance arc” may be substantially diluted by the surrounding emission. However, spectral sensitivity and photon statistics with Suzaku are quite high, which are important to determine the elemental abundance. One possible explanation is that the excess intensity of the hot ICM component in SW arc could have been mis-identified as the “high-abundance arc”.

We also note that the abundances were 0.35, 0.20, and 0.28 solar for $r < 1.1'$, NW arc, and SW arc, respectively, when the Suzaku spectra were fitted with the single absorbed *apec* model in the $0.7\text{--}7$ keV using the Grevesse & Sauval (1998) abundance just as performed by Gu et al. (2007). Though somewhat high abundance in SW arc was obtained, the abundance value was much lower than our results in table 5. Moreover, the model was rejected with high

statistical significance of $\chi^2/\text{dof} \sim 2$. The multi-phase nature of ICM is an important factor as discussed in section 6, and treating the data with a single temperature model can result in quite a different abundance value.

9. Extended Hard X-ray Emission

9.1. Observed Counts and NXB Reproducibility

The XIS spectra in figures 3(a)–(h) suggest hard X-ray emission in excess of the group thermal and LMXB emission in the energy range above ~ 5 keV. As already mentioned in section 4, the 6–10 keV hard-band image shows elongated feature along the NE and SW directions around the group center. It is partly because of a clump of point sources $\sim 1.5'$ aside the group center, but the feature looks to direct to the two cavities. Point source contribution at the group center is discussed later in this section. On the other hand, in the region at $r > 3.3'$ there seems no clear correlation with point sources. Since diffuse hard excess emission in HCG 62 was reported based on an ASCA observation (Fukazawa et al. 2001; Nakazawa et al. 2007), we investigate the properties of the hard emission with the Suzaku data.

Table 6 summarizes observed total counts compared with the expected contributions from background (NXB and CXB) and the group emission (ICM and LMXB). With statistics, the excess counts are significant by more than 3σ level in all the three annuli. We compared these results with the previous ASCA flux (Fukazawa et al. 2001; Nakazawa et al. 2007). Nakazawa et al. (2007) reported that the hard excess flux within 3–15' region was $0.92^{+0.18}_{-0.17} \times 10^{-12}$ erg cm $^{-2}$ s $^{-1}$ (2–10 keV), which is roughly $\sim 1/3$ of the CXB intensity. We calculated the expected counts with this flux assuming a spatially flat distribution. The results are shown in “ASCA” row in table 6. The present Suzaku counts look generally consistent with the ASCA results. However, systematics associated with the reproducibility of the NXB must be examined carefully.

Tawa et al. (2007) report that the intrinsic variability of NXB is 4.46/5.60/3.20% for XIS0/2/3 in 5–12 keV after the standard screening procedure. In this study, the NXB counts over 5 ks, which corresponds to 2–3 days of observation, was compared with an exposure weighted sum of the *COR* sorted data for night Earth observations. Therefore, the 90% confidence range of the NXB fluctuation for FI sensors is $1.6 \times \sqrt{(4.46^2 + 5.60^2 + 3.20^2)}/3 = 7.2 \pm 1.1\%$. They also claim that this level can be reduced to $6.5 \pm 1.0\%$ when an updated cut-off rigidity calculation of *COR2* is used as the NXB indicator and the following additional screening criteria are applied;

$$\begin{aligned}
& T_SAA_HXD > 436 \quad \text{AND} \\
& (SAT_LAT > -23 \quad \text{OR} \quad SAT_ALT < 576.5) \quad \text{AND} \\
& (SAT_LAT < +29 \quad \text{OR} \quad SAT_ALT < 577.5) \quad \text{AND} \\
& TIME \geq 181470000,
\end{aligned} \tag{2}$$

where *SAT_LAT* (deg) denotes the orbital location of the satellite in the geographic latitude, and *SAT_ALT* (km) is the altitude of the satellite. Though we have selected *COR* > 8 GV, which is different from the Tawa et al. (2007) study, we also tested the *COR2* sorted NXB estimation after the data screening with equation (2). The result was almost identical to the values in table 6, so that we adopt $\pm 6.5\%$ as the 90% confidence range of NXB systematic error for XIS-FI in 5–12 keV.

9.2. Outer Region and Study with HXD-PIN

Taking this NXB error into account, the excess hard counts in 3.3–6.5' and 6.5–9.8' annuli as shown in table 6(a) are no more significant. In figure 8, we plot the (OBS–NXB) spectra of the XIS-FI and HXD-PIN in comparison with the CXB, NXB, and ICM spectra. The XIS-FI spectrum in the 3.3–9.8' annulus exhibits an apparent excess over the nominal CXB spectrum by Kushino et al. (2002), however, it becomes quite consistent if the ICM and 6.5% NXB spectra are added (orange histogram). The observed counts above 12 keV shown in table 6(b) also suggests that the NXB counts are a few percent higher than our estimation. The effective area of the XRT above 12 keV is so small that almost all the observed counts should be due to the NXB, although the reproducibility in this energy band has not been studied.

In addition, the HXD-PIN data in 12–40 keV is fairly consistent with the nominal CXB spectrum, given by equation (1) of Gruber et al. (1999) in the energy range of 3–60 keV as;

$$S(E) = 7.877 E^{-0.29} \exp\left(-\frac{E}{41.13}\right) \frac{\text{keV}}{\text{keV cm}^2 \text{ s sr}}. \quad (3)$$

The residual counts after subtracting the official NXB events amounts to $(1.3 \pm 0.2 \pm 1.0) \times 10^{-2}$ cts s⁻¹ (15–40 keV). The former error stands for statistical 1 σ error, while the latter is a systematic error of $\sim 3.5\%$ (1 σ), derived from a document in the Suzaku web page.¹ We used the released response of the HXD-PIN for the HXD nominal position, `ae_hxd_pinhxnom_20060814.rsp`, and scaled by the opening angle of 0.3 deg² of “fine collimators” (Takahashi et al. 2007). The CXB contribution corrected for the normalization difference of 13% between XIS and PIN is derived as 1.9×10^{-2} cts s⁻¹, which agrees with the observed intensity if one takes into account the background systematics. Therefore, HXD-PIN shows no signature of strong excess hard X-rays in the 15–40 keV spectrum. If we take the PIN background systematics to be 5.6% at the 90% confidence, the upper limit on the flux is 6.2×10^{-12} erg cm⁻² s⁻¹ (15–40 keV).

9.3. Excess in Central Region

On the other hand, the 0.0–3.3' region shows significant excess counts with XIS-FI, even considering the uncertainty in the NXB flux. This region contains the cavities and possibly an X-ray weak AGN, together with four bright member galaxies (Zabludoff & Mulchaey 2000). As

¹ <http://www.astro.isas.jaxa.jp/suzaku/doc/suzakumemo/suzakumemo-2006-42.pdf>

shown in table 6(a), the estimated LMXB flux from these galaxies can account for only 30% of the observed excess after subtraction of the NXB, CXB, and ICM components. Even though the X-ray to optical luminosity ratio scatters by about 60% as indicated by equation (1), this scatter is unable to explain the whole excess flux.

The residual excess can be explained if there are more hard sources in excess of the nominal LMXBs in a similar order. To examine this, we looked into the high resolution Chandra image to directly measure the point source contribution. There are 17 sources cataloged by Harrison et al. (2003) in this region, and their locations are presented in figure 9 overlaid on the Chandra ACIS-S3 image with an exposure of 49.15 ks. The 2–10 keV fluxes of these sources distribute around $(0.7\text{--}8.2) \times 10^{-14}$ erg cm $^{-2}$ s $^{-1}$, which can be converted to a luminosity of $(3.3\text{--}39) \times 10^{39}$ erg s $^{-1}$, at the redshift of HCG 62. This luminosity range is higher than the level of typical LMXBs. We extracted the source spectra within $r < 3''$ and took the background from the 3–6'' annulus for each source. The combined spectrum, shown in figure 10, can be fitted well with a power-law model with $\Gamma = 1.38 \pm 0.06$, pretty consistent with the nominal CXB slope. However, the total flux amounts to $(2.81 \pm 0.24) \times 10^{-13}$ erg cm $^{-2}$ s $^{-1}$, which is higher than the expected CXB intensity, $\pi \cdot (3.3')^2 \cdot 5.97 \times 10^{-8}$ erg cm $^{-2}$ s $^{-1}$ sr $^{-1} = 1.73 \times 10^{-13}$ erg cm $^{-2}$ s $^{-1}$, by a factor of 1.62 ± 0.14 . This almost completely explains the relative excess flux of $70 \pm 19\%$ over the CXB as shown in table 6(a).

The point source contribution is much higher than the expected level, however it is still consistent with the CXB fluctuation. Kushino et al. (2002) reported a field-to-field intensity fluctuation of $\sigma_{\text{CXB}} = 6.5\%$, with a detector beam size of $\Omega \sim 0.4$ deg 2 in the 2–10 keV band with the ASCA GIS. Assuming a simple Euclidean log N -log S relation as $N(> S) \propto S^{-2.5}$, the CXB fluctuation scales as $\sigma_{\text{CXB}} \propto \Omega^{-0.5}$. This gives relative 1σ fluctuations of 42%, 25% and 19% for the 0.0–3.3', 3.3–6.5', and 6.5–9.8' annuli, respectively, so that the observed excess of $\sim 70\%$ at $r < 3.3'$ is within the 90% confidence range.

To summarize, there is a suggestion of extended hard X-ray emission reported by the ASCA GIS in the Suzaku XIS data. However, the uncertainties in the NXB and CXB prevent us from claiming significant detection. Some of the point sources detected with the Chandra ACIS-S3 may well be associated with HCG 62. Lastly, we warn that the hard excess flux increases by a large factor if we include all the XIS data, in particular with $COR \leq 8$ GV, in the spectral analysis, which is due certainly to the artificial effect of the NXB reproducibility. This indicates that suppression of the background counts with better screening criteria is essential in the analysis of such extended hard X-ray emission.

10. Discussion

10.1. High-Temperature Ring

We found the doughnut-like high-temperature ring at 3.3–6.5′ surrounding the group center, as shown in the hardness image of figure 1(b). Spectral fits, shown in figure 4(b), indicated an excess in the intensity ratio of hot to cool ICM components in this annulus. We note that the co-existence of the hot and cool components was already observed with Chandra and XMM-Newton (Morita et al. 2006) based on the deprojection analysis. However, as shown in figure 11(a) of Morita et al. (2006), the hot component should occupy more than $\gtrsim 90\%$ of the volume if two components are under a pressure balance. In other words, the total thermal energy given by a product of pressure and volume, PV , is dominated by the hot component in this annulus.

We therefore assume that the 3.3–6.5′ (60–120 kpc) annulus is filled with the hot ICM with temperature $kT_{\text{Hot}} \simeq 1.6$ keV and the electron density $n_e \simeq 7 \times 10^{-4} \text{ cm}^{-3}$ for simplicity. Then the gas pressure and the total energy are $P = 1.92 n_e kT_{\text{Hot}} = 2.2 \text{ eV cm}^{-3}$ and $E = PV = 5.8 \times 10^{59} \text{ erg s}^{-1}$, respectively. The bolometric luminosity is $L_{\text{bol}} = 1.1 \times 10^{42} \text{ erg s}^{-2}$ using the *vapec* model with the elemental abundances given in table 4 (Gal 2T) for this annulus. This gives the radiation cooling time as

$$\tau_{\text{cool}} = E/L_{\text{bol}} = 17 \text{ Gyr}, \quad (4)$$

which is longer than the Hubble time. The thermal conduction time is calculated as

$$\begin{aligned} \tau_{\text{cond}} &= r^2/\kappa_{\text{S}} = 0.33 \text{ Gyr} \\ &\times \left(\frac{r}{100 \text{ kpc}}\right)^2 \left(\frac{kT_{\text{Hot}}}{1.6 \text{ keV}}\right)^{-\frac{5}{2}} \left(\frac{n_e}{7 \cdot 10^{-4} \text{ cm}^{-3}}\right), \end{aligned} \quad (5)$$

assuming the Spitzer thermal conductivity (Spitzer 1962). Though this time scale is much shorter than the Hubble time, the thermal conduction may be suppressed by a large factor if there are turbulent magnetic fields, and the time scale may become comparable to or longer than the group age of a few Gyr.

Morita et al. (2006) suggest that the hydrostatic equilibrium is broken at $r \sim 5'$, and that the outflow of the hot ICM may occur, based on the result of steep temperature drop at $r \sim 5$ – $10'$. In this case, the hot ICM may be expanding with nearly the sound velocity, $v_s = \sqrt{\gamma kT_{\text{Hot}}/(\mu m_p)} = 640 \text{ km s}^{-1}$, where $\gamma = 5/3$ and $\mu = 0.62$. The expanding time scale is

$$\tau_s = r/v_s = 0.15 \left(\frac{r}{100 \text{ kpc}}\right) \left(\frac{kT_{\text{Hot}}}{1.6 \text{ keV}}\right)^{-0.5} \text{ Gyr}. \quad (6)$$

Thus, the total power input required to form the high-temperature ring can be roughly estimated as,

$$W = E/\tau_s = 1.2 \times 10^{44} \text{ erg s}^{-1}. \quad (7)$$

This power is by about two orders of magnitude higher than that required to generate the two cavities in the central region of HCG 62. The large implied power and the absence of strong AGN activity in this group suggest that the hot ring may be caused by some large-scale dynamical process in the central region of the group.

10.2. *Metallicity Distribution in ICM*

The present Suzaku observation of HCG 62 showed abundance distribution of O, Ne, Mg, Si, S, and Fe out to a radius of $10' \simeq 180$ kpc. Ne abundance has large ambiguity due to a strong coupling with Fe-L lines, as mentioned in section 7. Distributions of Mg, Si, S, and Fe are quite similar to each other, while O profile in the outer region has a large uncertainty. We plotted abundance ratios of O, Mg, Si, and S against Fe as a function of the projected radius in figure 11. Here, the values in the outermost region ($r > 9.8'$) were excluded because of large uncertainties. The ratios Mg/Fe, Si/Fe and S/Fe are consistent to be a constant value around 1.5–2, while O/Fe ratio for the innermost region ($r < 3.3'$) is significantly lower around 0.5. In the Gal 2T fit, the O/Fe ratio seems to increase with radius. These features have been seen with Chandra and XMM-Newton by Morita et al. (2006), and the present result gave a good confirmation in the outer region.

Recent Suzaku observations have presented abundance profiles in several other systems: an elliptical galaxy NGC 720 (Tawara et al. 2006), the Fornax cluster and NGC 1404 (Matsushita et al. 2007b), and a cluster of galaxies Abell 1060 (Sato et al. 2007). While Si/Fe ratio is almost the same among all the systems, Mg/Fe ratio is slightly higher in HCG 62 and Abell 1060 than in NGC 720, Fornax cluster, and NGC 1404. We compare the abundances in HCG 62 with those in the Fornax cluster as shown in figure 11. Regarding the Fornax cluster, we use $r_{180} = 1.00\sqrt{k\langle T \rangle / 1.3 \text{ keV}}$ Mpc, and $z = 0.00429$ corrected to the reference frame defined by the 3 K microwave background radiation (NASA/IPAC Extragalactic Database; NED). The solar abundance by Feldman (1992) with $[\text{Fe}/\text{H}] = 3.24 \times 10^{-5}$ employed by Matsushita et al. (2007b) was scaled by a factor of 0.7 to match the Anders & Grevesse (1989) value of $[\text{Fe}/\text{H}] = 4.68 \times 10^{-5}$. HCG 62 shows lower Fe abundance than the Fornax cluster in the central region at $r \lesssim 0.05 r_{180}$, but abundances become similar at $r \sim 0.1 r_{180}$. Abundance ratios of O/Fe, Mg/Fe, Si/Fe, and S/Fe are quite similar between HCG 62 and the Fornax cluster at $r \sim 0.1 r_{180}$.

Tamura et al. (2004) reported abundance ratios for 19 clusters studied with XMM-Newton, and the mean Si/Fe ratio in cool and medium temperature clusters with $kT < 6$ keV was ~ 1.4 , consistent with our HCG 62 result. Their O/Fe ratio, ~ 0.6 , in the cluster core also agrees with our result. Matsushita et al. (2003); Matsushita et al. (2007a) also reported abundance ratio for M87 and the Centaurus cluster, respectively. M87 showed the Mg/O ratio to be ~ 1.3 in the central region, and the Centaurus cluster indicated the O/Fe and Si/Fe ratios within $8'$ consistent with our results. The Mg/O ratio for HCG 62 with XMM-Newton (Morita

et al. 2006) is ~ 3.3 within $1'$, which is almost the same as our result of ~ 3.6 within $3.3'$. Mg/O ratios in other groups are ~ 2.5 for NGC 5044 (Tamura et al. 2003), and ~ 1.3 for NGC 4636 (Xu et al. 2002) both measured with XMM-Newton RGS.

Sato et al. (2007c) studied contributions of type Ia and II supernovae to the metal enrichment, based on Suzaku results of HCG 62, Abell 1060, AWM 7, NGC 570 (Sato et al. 2007; Sato et al. 2007b).

10.3. Metal Mass-to-Light Ratio

Metal mass-to-light ratios for oxygen, iron, and magnesium (OMLR, IMLR, and MMLR, respectively), were examined. First, we show the metal mass profiles in figure 12(a), based on the 3-dimensional gas mass profile by Morita et al. (2006) and the abundance profile measured with Suzaku. The derived iron mass within the 3-dimensional radius of $R < 200$ kpc is $(1.5\text{--}3) \times 10^8 M_\odot$, which is quite consistent with the previous measurement in figure 11(e) of Morita et al. (2006). We obtained the magnesium mass to be $(0.7\text{--}1.1) \times 10^8 M_\odot$. Though the oxygen mass has large errors as seen in figure 12(a), it is unlikely that oxygen has smaller mass than iron. Therefore, the Gal 2T model (crosses) is preferred to the Gal 1T one (solid and dotted lines). The estimated oxygen mass is $\sim 10^9 M_\odot$, within $R < 200$ kpc.

Secondly, we adopted Zabludoff & Mulchaey (2000) results as the member galaxy catalog of HCG 62 (12 galaxies in $r < 13' \sim 230$ kpc), and their redshifts were used to estimate the 3-dimensional distribution. Since only the R -band optical magnitudes are provided in this catalog, we converted them into the B -band magnitudes using the color of $B - R = 2.0$ mag for the HCG 62a galaxy at the center (Hickson et al. 1989), and $A_B = 0.224$ and $A_R = 0.139$ after NASA/IPAC Extragalactic Database (NED) in the direction of HCG 62.

We thus calculated the integrated values of OMLR, IMLR, and MMLR within $r \lesssim 230$ kpc as shown in figure 12(b), and they turned out to be $\sim 4 \times 10^{-2}$, $\sim 4.6 \times 10^{-3}$, and $\sim 1.5 \times 10^{-3} M_\odot/L_\odot$, respectively. The errors are only based on the statistical errors of metal abundances in the spectral fit, and the uncertainties of the gas mass profiles and the luminosities of the member galaxies are not considered. The IMLR values are consistent with the collective results with ASCA by Makishima et al. (2001). The MMLR and IMLR show similar steep increase with radius up to $r \sim 100$ kpc and seem to reach almost a plateau at 100–200 kpc. This feature is not apparent for the OMLR, due partly to the large uncertainty. The behavior of MLR curves would be related to different enrichment processes, as discussed in Morita et al. (2006).

We also point out that the derived OMLR and IMLR for HCG 62 are much larger than those of the Fornax cluster (Matsushita et al. 2007b) as shown in figure 12(b). Particularly the difference in IMLR is significant, although that in OMLR is marginal due to the uncertainty in the Galactic emission. These two systems have a similar potential depth with $k\langle T \rangle \sim 1.3$ keV. This feature may indicate that the Fornax cluster is a younger system with less number of

SN Ia for the Fe production since the cluster formation, and/or that the metal distribution in the Fornax may be much more extended. Possible difference of the initial mass function (IMF) between the two may account for some fraction of the discrepancy in the MLRs. Ikebe et al. (1996) discovered that there are two distinct length scales of dark matter concentration in the Fornax cluster, and the cD galaxy NGC 1399 is off-centered by ~ 50 kpc with respect to the cluster hot gas. There is also an X-ray luminous elliptical galaxy NGC 1404 at $10'$ south-west of NGC 1399. These features suggest that the Fornax system may be dynamically young and that galaxy interactions in ICM may have caused extended metal distribution.

10.4. AGN versus Mergers

HCG 62 exhibits several interesting activities in both the central and the outer regions: namely, two cavities (Vrtilek et al. 2002; Morita et al. 2006), extended hard X-ray emission (Fukazawa et al. 2001; Nakazawa et al. 2007), multi-phase ICM (Morita et al. 2006; this work), possible “high-abundance arc” (Gu et al. 2007), and the doughnut-like high-temperature ring (this work). One might relate the central features with an AGN activity, however, the central galaxy (HCG 62a = NGC 4761) currently shows little evidence of AGN activities in both optical (Coziol et al. 1998; Shimada et al. 2000; Coziol et al. 2004) and radio bands, as summarized in section 8.1 of Morita et al. (2006) and section 3.1 of Gu et al. (2007). Morita et al. (2006) also have placed an upper limit on the X-ray luminosity of the AGN to be $L_X \lesssim 10^{39}$ erg s $^{-1}$ (0.5–4 keV). Since the Suzaku HXD-PIN shows no excess over the CXB flux (figure 8), heavily absorbed AGN with an intrinsic luminosity larger than $\sim 3 \times 10^{42}$ erg s $^{-1}$ (15–40 keV) is also ruled out. Another possibility related with the HCG 62 activity can be recent mergers, as suggested in the above mentioned previous works. Energy inputs from magneto-hydrodynamic interactions of the member galaxies with the ICM (Makishima et al. 2001) can be another possible mechanism.

We found a concentration of hard sources in $r < 3.3'$ with average photon indices $\Gamma \sim 1.4$. As shown in section 8, this concentration itself is within the range of CXB fluctuation, however, the spatial coincidence with the group center is remarkable as seen in figure 1(b). Since the source luminosities are $(3.3\text{--}39) \times 10^{39}$ erg s $^{-1}$ (2–10 keV) at HCG 62, we suggest that some of the sources may be remnants of minor mergers which were previously central black holes of the merged galaxies. The overdensity of X-ray sources with $L_X = (4.0\text{--}250) \times 10^{39}$ erg s $^{-1}$ (2–10 keV) in the fields of A 194 and A 1060 was also reported by Hudaverdi et al. (2006). Optical identifications of these objects will be of much interest.

11. Summary

- Suzaku confirmed the multi-phase nature of the ICM out to a radius $\sim 10'$. We found a doughnut-like high-temperature ring at $3.3\text{--}6.5'$ in the hardness image, which is caused by higher hot component intensity over the cool component as shown by the spectral fit.

Possible ICM heating by the mass accretion is suggested.

- We could not confirm the “high-abundance arc” in SW arc in the 1.1–3.3′ annulus reported by Gu et al. (2007), and possible misidentification of an excess hot component as the line was suggested.
- Mg to Fe ratio showed enhancement at the center confirming the previous Chandra and XMM-Newton result. Temperature, surface brightness, and O abundance at $r > 3.3'$ were subject to modeling of the Galactic component, while Mg, Si, S, and Fe abundances were fairly robust. The Gal 2T model was preferred in terms of the surface brightness profile and the integrated O mass.
- O abundance was ~ 0.4 solar at the center and less than 0.5 at $r > 3.3'$. Abundance ratios, O/Fe, Mg/Fe, Si/Fe, and S/Fe, showed similar values with those in the Fornax cluster in $r \sim 0.1 r_{180}$. Comparison of 19 clusters with HCG 62 showed consistent levels of O/Fe ~ 0.6 and Si/Fe ~ 1.4 . On the other hand, HCG 62 showed Mg/O ~ 3.6 at $r < 3.3'$, significantly higher than in other groups and giant ellipticals.
- The OMLR and IMLR values in HCG 62 are by about order of magnitude higher than the Fornax cluster results at $r \sim 130$ kpc, while our IMLR agrees with collection of the ASCA results.
- Thermal fit and the 6–10 keV image indicated an excess above ~ 5 keV in most of the radii, however it was not significant considering uncertainties in the NXB and CXB fluctuations. ASCA detection of the hard excess is still consistent with our results.
- We found an excess X-ray emission of $70 \pm 19\%$ times the nominal CXB intensity (5–12 keV) within $r < 3.3'$, and most of it could be explained by a concentration of hard X-ray sources detected with Chandra. We suggested some of the sources could be remnants of minor mergers.

Part of this work was financially supported by the Ministry of Education, Culture, Sports, Science and Technology of Japan, Grant-in-Aid for Scientific Research No. 14079103, 15340088, 15001002, 16340077, 18740011.

References

- Anders, E., & Grevesse, N. 1989, *Geochim. Cosmochim. Acta*, 53, 197
- Borgani, S., Finoguenov, A., Kay, S. T., Ponman, T. J., Springel, V., Tozzi, P., & Voit, G. M. 2005, *MNRAS*, 361, 233
- Coziol, R., Ribeiro, A. L. B., Carvalho, R. R., & Capelato, H. V. 1998 *ApJ*, 493, 563
- Coziol, R., Brinks, E., & Bravo-Alfaro, H. 2004, *AJ*, 128, 68
- Dickey, J. M., & Lockman, F. J. 1990, *ARA&A*, 28, 215

- Evrard, A. E., Metzler, C. A., & Navarro, J. F. 1996, *ApJ*, 469, 494
- Feldman, U. 1992, *Phys. Scr.*, 46, 202
- Finoguenov, A., & Ponman, T. J. 1999, *MNRAS*, 305, 325
- Fukazawa, Y., Makishima, K., Tamura, T., Ezawa, H., Xu, H., Ikebe, Y., Kikuchi, K., & Ohashi, T. 1998, *PASJ*, 50, 187
- Fukazawa, Y., Nakazawa, K., Isobe, N., Makishima, K., et al. 2001, *ApJL*, 546, 87
- Grevesse, N., & Sauval, A. J. 1998, *Space Science Reviews*, 85, 161
- Gruber, D. E., Matteson, J. L., Peterson, L. E., & Jung, G. V. 1999, *ApJ*, 520, 124
- Gu, J., Xu, H., Gu, L., An, T., Wang, Y., Zhang, Z., & Wu, X.-P. 2007, *ApJ*, 659, 275
- Harrison, F. A., Eckart, M. E., Mao, P. H., Helfand, D. J., & Stern, D. 2003, *ApJ*, 596, 944
- Hickson, P., Kindl, E., & Auman, J. R. 1989, *ApJS*, 70, 687
- Hudaverdi, M., Kunieda, H., Tanaka, T., Haba, Y., Furuzawa, A., Tawara, Y., & Ercan, E. N. 2006, *PASJ*, 58, 931
- Ikebe, Y., et al. 1996, *Nature*, 379, 427
- Ishisaki, Y., et al. 2007, *PASJ*, 59, 113
- Kim, D.-W., & Fabbiano, G. 2004, *ApJ*, 611, 846
- Kokubun, M., et al. 2007, *PASJ*, 59, 53
- Koyama, K., et al. 2007, *PASJ*, 59, 23
- Kushino, A., Ishisaki, Y., Morita, U., Yamasaki, N. Y., Ishida, M., Ohashi, T., & Ueda, Y. 2002, *PASJ*, 54, 327
- Kuntz, K. D., & Snowden, S. L. 2000, *ApJ*, 543, 195
- Lodders, K. 2003, *ApJ*, 591, 1220
- Snowden, S. L., et al. 1995, *ApJ*, 454, 643
- Lumb, D. H., Warwick, R. S., Page, M., & De Luca, A. 2002, *A&A*, 389, 93
- Makishima, K., et al. 2001, *PASJ*, 53, 401
- Markevitch, M., et al. 1998, *ApJ*, 503, 77
- Matsushita, K., Finoguenov, A., Böhringer, H. 2003, *A&A*, 401, 443
- Matsushita, K., Böhringer, H., Takahashi, I., & Ikebe, Y. 2007, *A&A*, 462, 953
- Matsushita, K., et al. 2007, *PASJ*, 59, 327
- Morita, U., Ishisaki, Y., Yamasaki, N. Y., Ota, N., Kawano, N., Fukazawa, Y., & Ohashi, T. 2006, *PASJ*, 58, 719
- Mulchaey, J. S., Davis, D. S., Mushotzky, R. F., & Burstein, D. 2003, *ApJS*, 145, 39
- Nakazawa, K., Makishima, K., & Fukazawa, Y. 2007, *PASJ*, 59, 167
- Navarro, J. F., Frenk, C. S., & White, S. D. M. 1995, *MNRAS*, 275, 720
- Pildis, R. A., Bregman, J. N., & Evrard, A. E. 1995, *ApJ*, 443, 514
- Ponman, T. J., & Bertram, D. 1993, *Nature*, 363, 51
- Ponman, T. J., Cannon, D. B., & Navarro, J. F. 1999, *Nature*, 397, 135
- Rampazzo, R., Covino, S., Trinchieri, G., & Reduzzi, L. 1998, *A&A*, 330, 423
- Sato, K., et al. 2007, *PASJ*, 59, 299
- Sato, K., et al. 2007b, *PASJ*, in press [arXiv:0707.4342]

- Sato, K., Tokoi, K., Matsushita, K., Ishisaki, Y., Yamasaki, N. Y., Ishida, M., & Ohashi, T. 2007, ApJL, 667, L41
- Serlemitsos, P. J., et al. 2007, PASJ, 59, 9
- Shimada, M., Ohyama, Y., Nishiura, S., Murayama, T., & Taniguchi, Y. 2000, AJ, 119, 2664
- Snowden, S. L., Egger, R., Freyberg, M. J., McCammon, D., Plucinsky, P. P., Sanders, W. T., Schmitt, J. H. M. M., Truemper, J. and Voges, W. 1998, ApJ, 493, 715
- Spavone, M., Iodice, E., Longo, G., Paolillo, M., & Sodani, S. 2006, A&A, 457, 493
- Spitzer, L. 1962, Physics of Fully Ionized Gases (2nd ed.; New York: Wiley)
- Takahashi, T., et al. 2007, PASJ, 59, 35
- Tamura, T., Kaastra, J. S., Makishima, K., & Takahashi, I. 2003, A&A, 399, 497
- Tamura, T., Kaastra, J. S., den Herder, J. W. A., Bleeker, J. A. M., & Peterson, J. R. 2004, A&A, 420, 135
- Tawa, N., et al. 2007, PASJ, submitted
- Tawara, Y., et al. 2007, PASJ, in press
- Uchiyama, Y., 2007, PASJ, in press
- Vrtilek, J. M., Grego, L., David, L. P., Ponman, T. J., Forman, W., Jones, C., & Harris, D. E. 2002, APS Meeting Abstracts, 17107
- Xu, H., et al. 2002, ApJ, 579, 600
- Zabludoff, A. I., & Mulchaey, J. S. 2000, ApJ, 539, 136

Table 4. Summary of the best-fit parameters for single (Gal 1T) or two (Gal 2T) temperature Galactic component models.

| Gal 1T | kT_{Hot} (keV) | kT_{Cool} (keV) | O (solar) | Ne (solar) | Mg, Al (solar) | Si (solar) | S, Ar, Ca (solar) | Fe, Ni (solar) | χ^2/dof | | | |
|----------|----------------------------|-----------------------------|------------------------|------------------------|--------------------------|-------------------------|---------------------------|----------------------------|---------------------------|---------------------------|----------------------------|----------------------------|
| 0.0–3.3′ | $1.65^{+0.03}_{-0.03}$ | $0.766^{+0.007}_{-0.007}$ | $0.32^{+0.08}_{-0.07}$ | $1.66^{+0.24}_{-0.22}$ | $1.24^{+0.14}_{-0.12}$ | $0.97^{+0.07}_{-0.07}$ | $1.12^{+0.13}_{-0.12}$ | $0.82^{+0.06}_{-0.05}$ | 654/473 | | | |
| 3.3–6.5′ | $1.48^{+0.06}_{-0.06}$ | $0.753^{+0.027}_{-0.031}$ | $0.10^{+0.13}_{-0.10}$ | $0.55^{+0.18}_{-0.17}$ | $0.36^{+0.11}_{-0.10}$ | $0.32^{+0.07}_{-0.06}$ | $0.38^{+0.10}_{-0.10}$ | $0.26^{+0.03}_{-0.03}$ | 512/421 | | | |
| 6.5–9.8′ | $1.23^{+0.06}_{-0.05}$ | $0.588^{+0.048}_{-0.062}$ | $0.00^{+0.10}_{-0.00}$ | $0.04^{+0.16}_{-0.04}$ | $0.22^{+0.10}_{-0.09}$ | $0.20^{+0.07}_{-0.07}$ | $0.41^{+0.14}_{-0.13}$ | $0.17^{+0.02}_{-0.02}$ | 467/405 | | | |
| 9.8–13′ | $1.43^{+0.20}_{-0.17}$ | $0.301^{+0.060}_{-0.043}$ | $0.07^{+0.08}_{-0.06}$ | $0.72^{+0.34}_{-0.26}$ | $0.41^{+0.56}_{-0.39}$ | $0.39^{+0.51}_{-0.39}$ | $0.00^{+0.54}_{-0.00}$ | $0.25^{+0.19}_{-0.12}$ | 301/285 | | | |
| All | | | | | | | | | 1934/1584 | | | |
| Gal 2T | kT_{Hot} (keV) | kT_{Cool} (keV) | O (solar) | Ne (solar) | Mg, Al (solar) | Si (solar) | S, Ar, Ca (solar) | Fe, Ni (solar) | χ^2/dof | | | |
| 0.0–3.3′ | $1.66^{+0.03}_{-0.03}$ | $0.773^{+0.007}_{-0.007}$ | $0.35^{+0.08}_{-0.08}$ | $1.71^{+0.25}_{-0.23}$ | $1.29^{+0.14}_{-0.13}$ | $1.01^{+0.10}_{-0.09}$ | $1.16^{+0.13}_{-0.12}$ | $0.84^{+0.06}_{-0.06}$ | 657/473 | | | |
| 3.3–6.5′ | $1.63^{+0.17}_{-0.12}$ | $0.990^{+0.060}_{-0.114}$ | $0.23^{+0.14}_{-0.13}$ | $0.36^{+0.24}_{-0.25}$ | $0.39^{+0.13}_{-0.11}$ | $0.35^{+0.08}_{-0.07}$ | $0.38^{+0.11}_{-0.10}$ | $0.29^{+0.04}_{-0.04}$ | 500/421 | | | |
| 6.5–9.8′ | $1.81^{+0.28}_{-0.31}$ | $1.047^{+0.036}_{-0.074}$ | $0.15^{+0.17}_{-0.15}$ | $0.00^{+0.15}_{-0.00}$ | $0.25^{+0.15}_{-0.13}$ | $0.20^{+0.09}_{-0.08}$ | $0.36^{+0.16}_{-0.16}$ | $0.20^{+0.05}_{-0.05}$ | 451/405 | | | |
| 9.8–13′ | $1.02^{+0.06}_{-0.06}$ | ———— | $0.38^{+0.38}_{-0.30}$ | $0.00^{+0.26}_{-0.00}$ | $0.00^{+0.20}_{-0.00}$ | $0.11^{+0.22}_{-0.11}$ | $0.00^{+0.45}_{-0.00}$ | $0.11^{+0.04}_{-0.03}$ | 311/287 | | | |
| All | | | | | | | | | 1919/1586 | | | |
| Gal 1T | kT_{Gal} (keV) | | K_{Hot}^* | K_{Cool}^* | K_{Gal}^\dagger | | S_{Hot}^\ddagger | S_{Cool}^\ddagger | S_{Gal}^\ddagger | S_{CXB}^\ddagger | S_{LMXB}^\ddagger | |
| 0.0–3.3′ | ↓ | | $32.6^{+1.6}_{-1.6}$ | $30.3^{+1.9}_{-1.9}$ | ↓ | | 23.3 | 43.5 | ↓ | ↓ | 0.9 | |
| 3.3–6.5′ | ↓ | | $11.9^{+0.8}_{-0.8}$ | $4.1^{+0.5}_{-0.4}$ | ↓ | | 6.2 | 2.7 | ↓ | ↓ | — | |
| 6.5–9.8′ | ↓ | | $9.6^{+0.8}_{-0.9}$ | $3.1^{+0.6}_{-0.5}$ | ↓ | | 4.5 | 1.4 | ↓ | ↓ | — | |
| 9.8–13′ | $0.208^{+0.007}_{-0.011}$ | | $4.4^{+1.0}_{-0.9}$ | $5.6^{+1.5}_{-1.4}$ | $1.2^{+0.1}_{-0.1}$ | | 2.3 | 2.2 | 1.8 | 1.6 | — | |
| Gal 2T | kT_{G1} (keV) | kT_{G2} (keV) | K_{Hot}^* | K_{Cool}^* | K_{G1}^\dagger | K_{G2}^\dagger | S_{Hot}^\ddagger | S_{Cool}^\ddagger | S_{G1}^\ddagger | S_{G2}^\ddagger | S_{CXB}^\ddagger | S_{LMXB}^\ddagger |
| 0.0–3.3′ | ↓ | ↓ | $31.8^{+1.6}_{-1.6}$ | $29.2^{+1.9}_{-1.9}$ | ↓ | ↓ | 22.9 | 43.0 | ↓ | ↓ | ↓ | 0.9 |
| 3.3–6.5′ | ↓ | ↓ | $9.1^{+1.8}_{-1.7}$ | $5.3^{+2.1}_{-2.0}$ | ↓ | ↓ | 4.8 | 3.3 | ↓ | ↓ | ↓ | — |
| 6.5–9.8′ | ↓ | ↓ | $4.0^{+1.9}_{-0.8}$ | $5.9^{+1.9}_{-1.9}$ | ↓ | ↓ | 1.9 | 3.1 | ↓ | ↓ | ↓ | — |
| 9.8–13′ | 0.138 (fix) | 0.344 (fix) | ———— | $7.5^{+1.3}_{-1.2}$ | $1.3^{+0.1}_{-0.1}$ | $0.9^{+0.1}_{-0.1}$ | — | 3.5 | 1.2 | 1.5 | 1.6 | — |

* Normalization of the *vapec* component scaled with a factor of SOURCE_RATIO_REG / AREA in table 2,

$K = \frac{\text{SOURCE_RATIO_REG}}{\text{AREA}} \int n_e n_H dV / (4\pi(1+z)^2 D_A^2) \times 10^{-20} \text{ cm}^{-5} \text{ arcmin}^{-2}$, where D_A is the angular distance to the source.

† Normalization of the *apec* component divided by the solid angle, $\Omega^U = \pi \times (20')^2$, assumed in the uniform-sky ARF calculation (20' radius from the optical axis of each XIS sensor), $K = \int n_e n_H dV / (4\pi(1+z)^2 D_A^2) / \Omega^U \times 10^{-20} \text{ cm}^{-5} \text{ arcmin}^{-2}$.

‡ Surface brightness in 0.4–4 keV in unit of photons $\text{cm}^{-2} \text{ Ms}^{-1} \text{ arcmin}^{-2}$, calculated in the same way as the normalization, and corrected for the Galactic absorption of $N_H = 3.03 \times 10^{20} \text{ cm}^{-2}$.

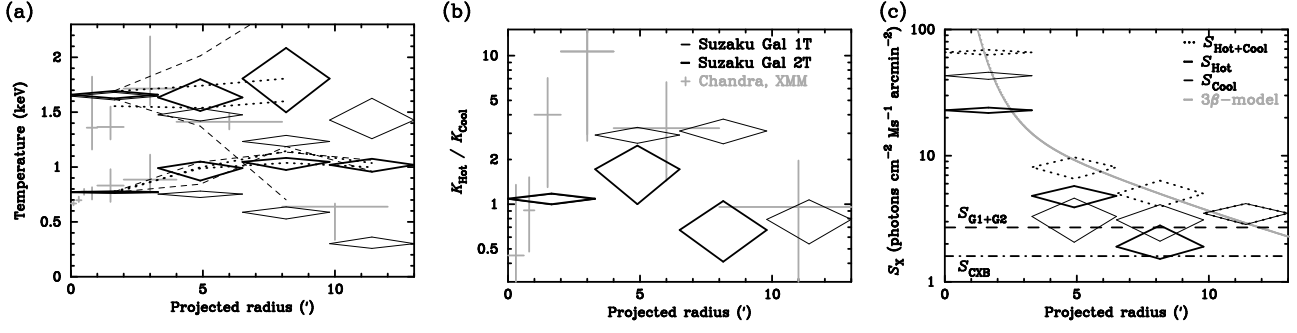


Fig. 4. (a) Temperatures of the ICM components, kT_{Hot} and kT_{Cool} , (b) ratio of the hot ICM component normalization to the cool ICM, $K_{\text{Hot}} / K_{\text{Cool}}$, and (c) surface brightness profiles corrected for the Galactic absorption, are plotted against radii from the group center. Diamonds in thin lines represent the Suzaku best-fit results with the Gal 1T model and diamonds in thick lines represents the results with the Gal 2T model in (a) and (b). Only the result with the Gal 2T model is presented in (c). Dashed lines in (a) denote the movable range of the best-fit temperature when the NXB + CXB components are changed by $\pm 10\%$, and dotted lines denote the range when the absorption column of the XIS contaminant is changed by $\pm 20\%$. Gray crosses in (a), (b) and the gray line (3β -model) in (c) are adopted from the previous results with Chandra and XMM-Newton by Morita et al. (2006).

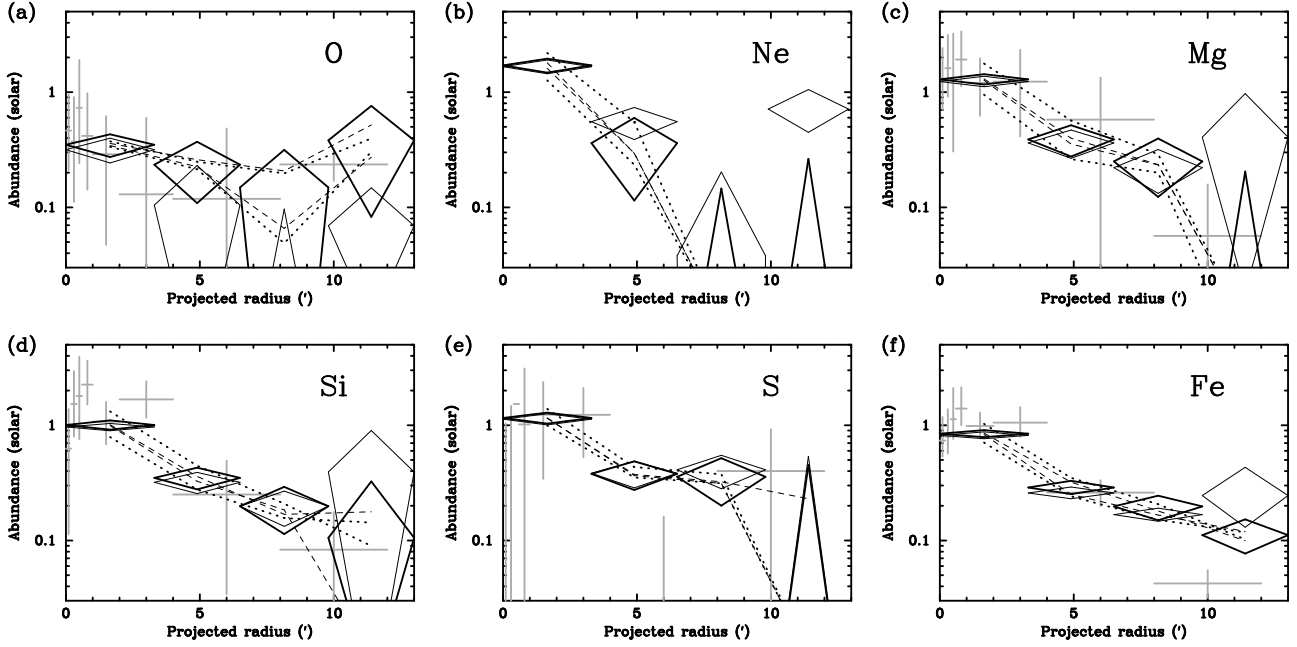


Fig. 5. Elemental abundances are plotted against radii from the group center. Diamonds in thin lines represents the Suzaku best-fit results with the Gal 1T model and diamonds in thick lines represents the results with the Gal 2T model. Dashed lines denote the movable range of the best-fit temperature when the NXB + CXB components are changed by $\pm 10\%$, and dotted lines denote the range when the absorption column of the XIS contaminant is changed by $\pm 20\%$. Gray crosses are adopted from the previous results with Chandra and XMM-Newton by Morita et al. (2006), in which Ne was fixed to have the same value with the O abundance.

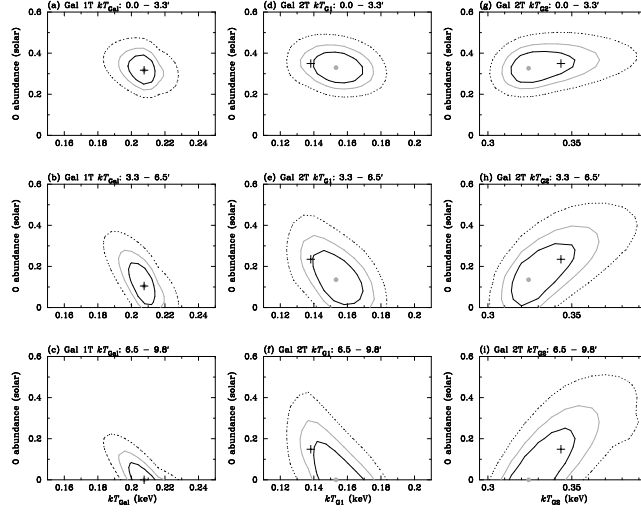


Fig. 6. Confidence contours between O abundance of the ICM component and temperature of the Galactic component with the Gal 1T model for (a)–(c), and with the Gal 2T model for (d)–(i). The contours represents 1σ , 90%, and 99% confidence regions from inner to outer, corresponding $\Delta\chi^2 = +2.3$, $+4.6$, and $+9.21$ from the χ^2 -minimum. The cross markers represents the best-fit locations in table 4, while the filled gray circles represents the χ^2 -minimum, which are different from the best-fit for the Gal 2T model because the temperatures of the *apex* models were fixed in the fitting whereas kT_{G1} or kT_{G2} was allowed to change in these plots.

Table 5. Best-fit parameters for spectra in $r < 1.1'$, NE arc, and SW arc with Gal 2T model.

| Gal 2T | kT_{Hot} (keV) | kT_{Cool} (keV) | O (solar) | Ne (solar) | Mg, Al (solar) | Si (solar) | S, Ar, Ca (solar) | Fe, Ni (solar) | χ^2/dof |
|------------|----------------------------|-----------------------------|------------------------|------------------------|------------------------|------------------------|------------------------|------------------------|---------------------|
| $r < 1.1'$ | $1.63^{+0.06}_{-0.06}$ | $0.755^{+0.009}_{-0.009}$ | $0.45^{+0.17}_{-0.14}$ | $1.99^{+0.52}_{-0.45}$ | $1.80^{+0.19}_{-0.29}$ | $1.42^{+0.15}_{-0.14}$ | $1.66^{+0.29}_{-0.26}$ | $1.22^{+0.18}_{-0.15}$ | 549/473 |
| NE arc | $1.74^{+0.08}_{-0.09}$ | $0.778^{+0.012}_{-0.015}$ | $0.31^{+0.15}_{-0.13}$ | $1.76^{+0.40}_{-0.44}$ | $1.23^{+0.25}_{-0.24}$ | $0.96^{+0.18}_{-0.17}$ | $0.84^{+0.22}_{-0.20}$ | $0.71^{+0.10}_{-0.10}$ | 545/473 |
| SW arc | $1.55^{+0.05}_{-0.05}$ | $0.785^{+0.013}_{-0.013}$ | $0.37^{+0.16}_{-0.14}$ | $1.65^{+0.45}_{-0.41}$ | $1.34^{+0.25}_{-0.23}$ | $1.00^{+0.17}_{-0.15}$ | $1.26^{+0.23}_{-0.21}$ | $0.86^{+0.11}_{-0.10}$ | 520/473 |

| Gal 2T | kT_{G1} (keV) | kT_{G2} (keV) | K_{Hot} | K_{Cool} | K_{G1} | K_{G2} | S_{Hot} | S_{Cool} | S_{G1} | S_{G2} | S_{CXB} | S_{LMXB} |
|------------|---------------------------|---------------------------|----------------------|-----------------------|-----------------|-----------------|------------------|-------------------|-----------------|-----------------|------------------|-------------------|
| $r < 1.1'$ | 0.138 (fix) | 0.344 (fix) | $91.2^{+9.8}_{-9.5}$ | $138.0^{+18.}_{-17.}$ | 1.3 (fix) | 0.9 (fix) | 77.8 | 274.2 | 1.2 | 1.5 | 1.6 | 0.9 |
| NE arc | ↑ | ↑ | $14.3^{+1.4}_{-1.1}$ | $12.1^{+1.6}_{-1.4}$ | ↑ | ↑ | 9.4 | 15.8 | ↑ | ↑ | ↑ | ↑ |
| SW arc | ↑ | ↑ | $17.1^{+1.5}_{-1.4}$ | $10.1^{+1.1}_{-1.0}$ | ↑ | ↑ | 13.1 | 14.9 | ↑ | ↑ | ↑ | ↑ |

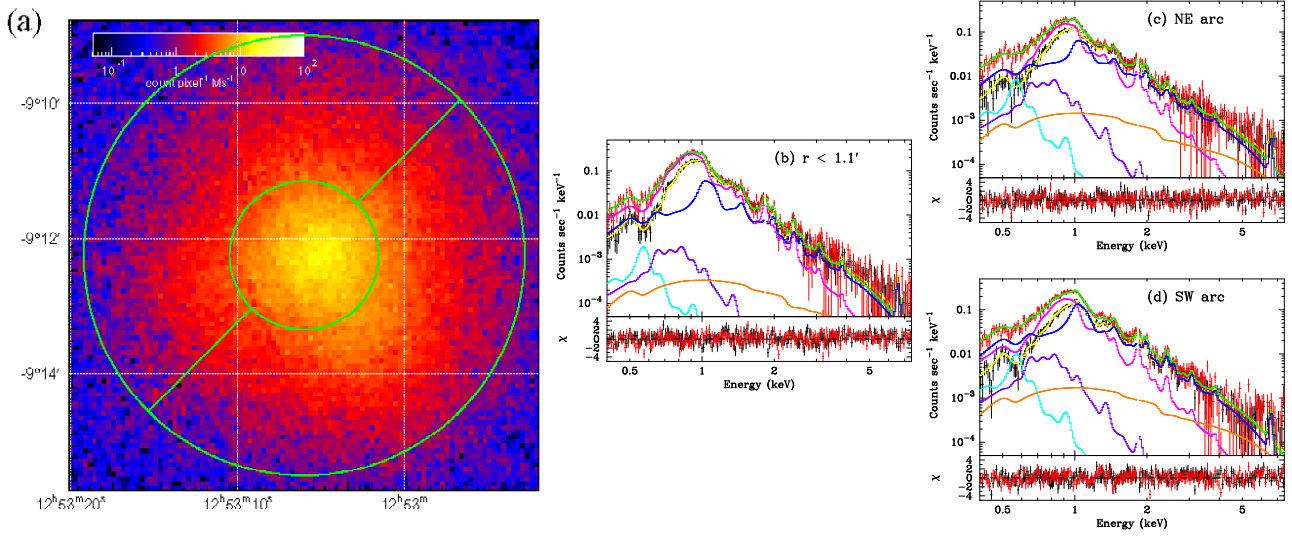


Fig. 7. (a) Magnification of the 0.0–3.3' annulus in figure 1(a), which is divided into three regions of $r < 1.1'$, NE arc, and SW arc. The image is binned to $4.2'' \times 4.2''$, and the smoothing with gaussian is not conducted. (b)–(d) Energy spectra of the three regions.

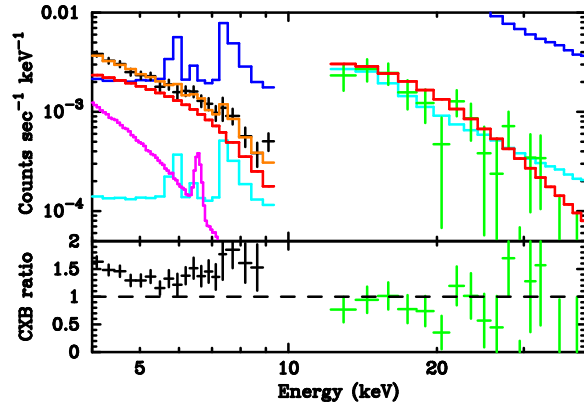


Fig. 8. The 4–10 keV band XIS spectrum of FI sensors (black) at 3.3–9.8' annulus and the 12–40 keV band spectrum of HXD-PIN (green). The estimated NXB spectra (blue) are subtracted from both spectra, but the CXB spectra (red) are not subtracted. The ICM component for XIS is shown by magenta line, and the 90% confidence levels of the NXB reproducibility for XIS ($\pm 6.5\%$) and HXD-PIN ($\pm 5.6\%$) are indicated by cyan histograms. The orange histogram represents the ICM + CXB + 6.5% NXB spectrum for XIS. Bottom panel show the ratio of each spectrum to CXB.

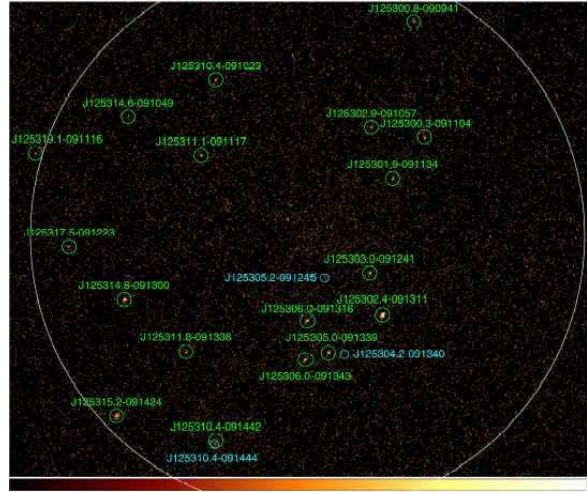


Fig. 9. The 2–10 keV band image of the central region of HCG 62 obtained with Chandra ACIS-S3 with 49.15 ks exposure. A large white circle represents 3.3' radius from the group center. Point sources detected in 2.1–7 keV are indicated by small green circles, and cyan circles correspond to sources only detected in 0.3–2.1 keV (Harrison et al. 2003).

Table 6. Summary of counts in (a) 5–12 keV and (b) above 12 keV bands with the XIS FI sensors (XIS0 + XIS2 + XIS3) under the condition of $COR > 8$ GV with 85.4 ks exposure.

| (a) Counts in 5–12 keV | | | |
|------------------------|---------------|-----------------|-----------------|
| Region | 0.0–3.3′ | 3.3–6.5′ | 6.5–9.8′ |
| OBS * | 2619 | 5759 | 7396 |
| NXB † | 1451 | 4298 | 5944 |
| CXB † | 420 | 989 | 905 |
| ICM ‡ | 333 | 180 | 90 |
| LMXB ‡ | 121 | — | — |
| Excess § | 294 ± 82 | 292 ± 121 | 420 ± 138 |
| NXB fraction | $21 \pm 6\%$ | $6.8 \pm 2.8\%$ | $7.1 \pm 2.3\%$ |
| CXB fraction | $70 \pm 19\%$ | $30 \pm 12\%$ | $46 \pm 15\%$ |
| ASCA # | 140 | 330 | 302 |

| (b) Counts above 12 keV | | | |
|-------------------------|-----------------|-----------------|-----------------|
| Region | 0.0–3.3′ | 3.3–6.5′ | 6.5–9.8′ |
| OBS * | 598 | 1787 | 2318 |
| NXB † | 546 | 1650 | 2182 |
| CXB † | 4 | 5 | 4 |
| Excess § | 48 ± 39 | 132 ± 68 | 132 ± 77 |
| NXB fraction | $8.8 \pm 7.1\%$ | $8.0 \pm 4.1\%$ | $6.0 \pm 3.5\%$ |

* Observed counts with FI sensors including the NXB and CXB.

† Estimated NXB and CXB counts presented in figure 2.

‡ ICM and LMXB counts for the Gal-2T model in table 4.

§ Excess \equiv OBS – NXB – CXB – ICM – LMXB, and the 90% confidence Poisson error calculated as $1.6 \times \sqrt{\text{OBS}}$.

|| NXB or CXB fraction calculated as $\frac{\text{Excess}}{\text{NXB}}$ or $\frac{\text{Excess}}{\text{CXB}}$.

Predicted excess hard counts by the ASCA results, as $\frac{\text{CXB}}{3}$.

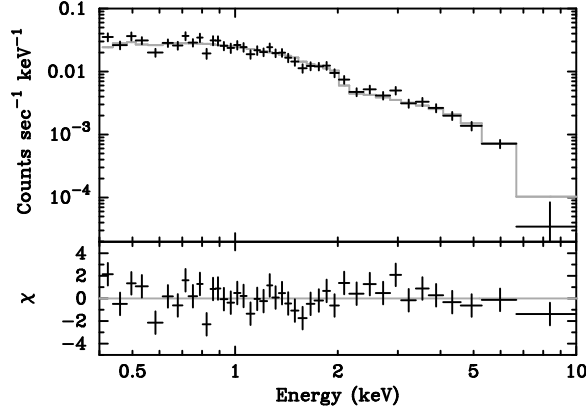


Fig. 10. Summed spectra of 17 point sources detected with Chandra ACIS-S within $r < 3.3'$ from the group center. The gray histogram represents the best-fit power-law model multiplied by the Galactic absorption of $N_{\text{H}} = 3.03 \times 10^{20} \text{ cm}^{-2}$. The best-fit parameters are a photon index, $\Gamma = 1.38 \pm 0.06$, and 2–10 keV flux, $F_{\text{X}} = (2.81 \pm 0.24) \times 10^{-13} \text{ erg cm}^{-2} \text{ s}^{-1}$, with $\chi^2/\text{dof} = 44.6/40$. The power-law model is acceptable with null hypothesis probability of 0.283. The bottom panel shows the fit residuals in unit of σ .

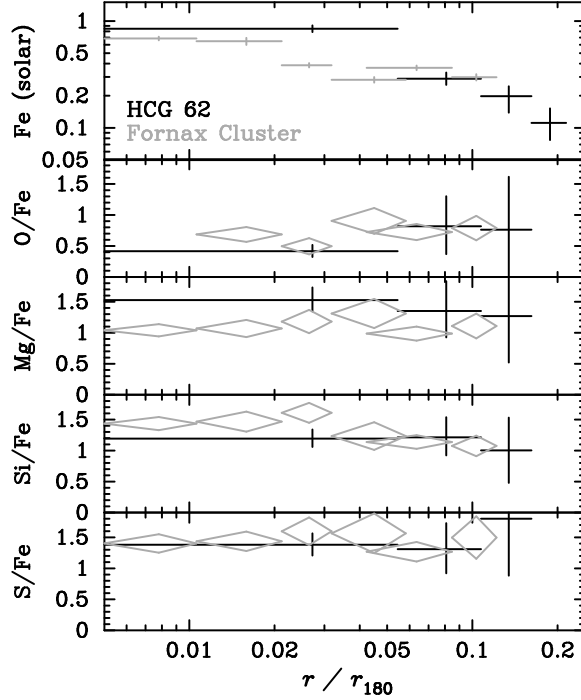


Fig. 11. Comparison of the Gal 2T results for HCG 62 (black) with results for the Fornax cluster (gray; Matsushita et al. 2007b). Fe abundance and the O/Fe, Mg/Fe, Si/Fe, and S/Fe ratios in solar unit (Anders & Grevesse 1989) are plotted against the projected radius scaled by the virial radius, r_{180} , from upper to lower panels. Results in $r > 9.8'$ for HCG 62 are not plotted for the Fe ratios due to the large uncertainty. The innermost point of the O/Fe ratio is not plotted because of the unsatisfactory fit.

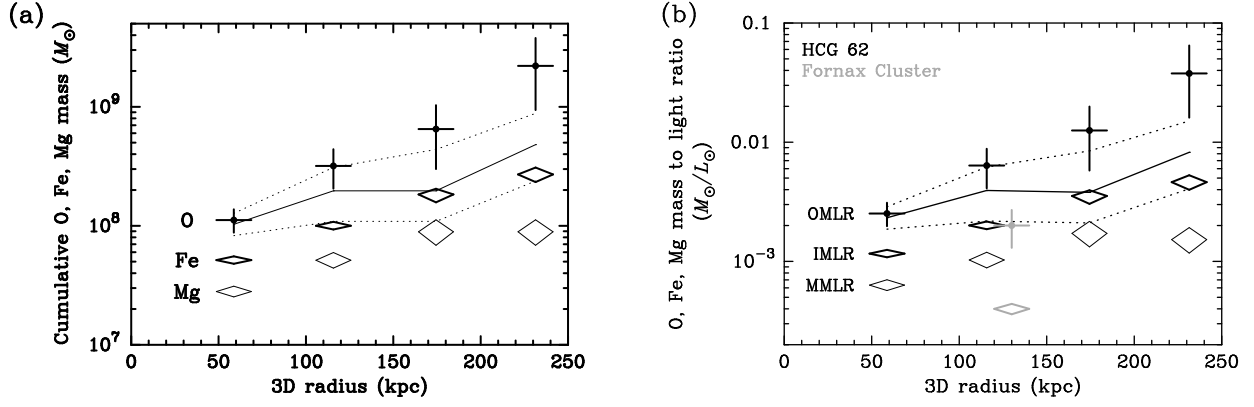


Fig. 12. (a) Cumulative mass, $M(< R)$, within the 3-dimensional radius, R , for O, Fe, and Mg are plotted for HCG 62, combining the abundance determination with Suzaku and the gas mass profile with Chandra and XMM-Newton. The cross and diamond markers show the mass profiles with the Gal 2T model, and the O mass profile and its error region with the Gal 1T model are shown in solid and dotted lines. (b) Ratios of the oxygen, iron, and magnesium mass in unit of M_{\odot} to the B band optical luminosity in unit of L_{\odot} (OMLR, IMLR, and MMLR, respectively) are plotted against the 3-dimensional radius. Black markers represent our results for HCG 62, and gray markers of OMLR and IMLR show the results for the Fornax cluster by Matsushita et al. (2007b).